sensors

MDPI

*Article*

# Enhanced Sensing Enabled by Multi-Resonant QBIC-EIT and SP-BIC in Pyramidal $LiNbO_3$ Metasurfaces

**Changqing Zhong [1], Wei Zou [1], Jiangtao Lei [2], Yun Shen [1,2], Jing Chen [3,*], Lujun Hong [2,*] and Tianjing Guo [2,*]**

[1] Department of Physics, School of Physics and Material Science, Nanchang University, Nanchang 330031, China; 402200230064@email.ncu.edu.cn (C.Z.); 352200250005@email.ncu.edu.cn (W.Z.); shenyun@ncu.edu.cn (Y.S.)
[2] Institute of Space Science and Technology, Nanchang University, Nanchang 330031, China; jiangtaolei@ncu.edu.cn
[3] School of Physics, Nankai University, Tianjin 300071, China
* Correspondence: jchen4@nankai.edu.cn (J.C.); ljhong@ncu.edu.cn (L.H.); tianjing@ncu.edu.cn (T.G.)

**Abstract**

In optical sensing, electromagnetically induced transparency (EIT) and bound states in the continuum (BIC) substantially enhance light–matter interactions by leveraging high-Q resonances. This study theoretically demonstrates dual-resonance phenomena—namely, a quasi-symmetry-protected BIC (SP-BIC) and a quasi-BIC-induced EIT-like (QBIC-EIT) resonance—using a dielectric metasurface composed of pyramid-shaped lithium niobate nanoarrays operating in the near-infrared. The QBIC-EIT transmission window originates from the interference between surface lattice modes and toroidal dipole modes, triggered by symmetry breaking of the BIC state. Due to the absence of $C_{4v}$ rotational symmetry in the pyramidal unit cells, the metasurface exhibits pronounced polarization-dependent responses: Under x-polarized incidence, a single quasi-SP-BIC resonance appears; under y-polarization, dual quasi-SP-BIC resonances along with a distinct QBIC-EIT resonance are observed. Both the high-Q quasi-SP-BIC resonance and the EIT-like window show strong sensitivity to changes in the ambient refractive index (RI). Specifically, the EIT-like window achieves a sensitivity of 404.9 nm/RIU, while the quasi-SP-BIC resonance delivers an exceptional sensitivity of 887.7 nm/RIU, confirming the metasurface's performance as a high-sensitivity RI sensor. These findings establish a multi-band detection platform for advanced RI sensing and contribute to the development of high-performance metasurface-based optical sensors.

**Keywords:** bound states in the continuum (BIC); electromagnetically induced transparency (EIT); high Q-factor; refractive index (RI) sensing; lithium niobate (LN) metasurfaces

Check for updates

Academic Editor: Guowen Ding

Received: 19 March 2026
Revised: 17 April 2026
Accepted: 21 April 2026
Published: 24 April 2026

**Copyright:** © 2026 by the authors. Licensee MDPI, Basel, Switzerland. This article is an open access article distributed under the terms and conditions of the Creative Commons Attribution (CC BY) license.

## 1. Introduction

The advancement of nanophotonics is significantly driven by leveraging optical resonances to achieve exceptionally high radiative quality factors (Q-factors) [1]. A key phenomenon in this domain is electromagnetically induced transparency (EIT) [2,3], a coherent linear optical effect [4] initially observed in laser-driven three-level atomic systems under cryogenic conditions [5–7]. EIT manifests as a narrow transparency window within an absorption spectrum, arising from quantum interference effects [8], and holds substantial promise for diverse photonic applications [9–11]. However, its practical implementation in atomic systems is hindered by stringent requirements, including cryogenic temperatures [12], coherent pumping [6], and high optical intensities [13]. Recently, the

demonstration of EIT-like behavior in plasmonic metamaterials has provided a more accessible pathway [14,15]. These structures enable EIT realization using incoherent light at room temperature. Consequently, plasmonic EIT metamaterials have found applications in slow-light devices, active plasmonic switching, and biological/chemical sensing [16–21]. Nevertheless, their performance is fundamentally limited by high intrinsic ohmic losses and irreversible photothermal conversion, leading to significantly constrained Q-factors [18]. To circumvent the substantial ohmic losses inherent in metallic structures, all-dielectric metasurfaces have emerged as a highly promising alternative [22,23]. EIT effects realized in such dielectric platforms offer advantages for low-loss slow-light devices, optical storage, and nonlinear optics [24–26]. Crucially, they exhibit significant potential for advanced refractive index (RI) sensing, where both sensitivity and figure of merit (FOM) are critical performance metrics [27–29].

Concurrently, bound states in the continuum (BICs) have garnered considerable attention in optical metasurface design confinement at the nanoscale [30–32]. BICs can be classified as symmetry-protected BICs (SP-BICs) or accidental BICs, distinguished by the mechanism decoupling their eigenmodes from the radiative continuum [33–35]. SP-BICs arise from specific structural symmetries (e.g., rotational or reflection symmetry) and can be transformed into observable Quasi-BICs (QBICs) with finite, yet high, Q-factors by intentionally breaking this symmetry to introduce controlled coupling to radiation [36,37]. Accidental BICs, conversely, stem from destructive interference between radiative channels [38]. High-Q BIC metasurfaces hold great promise for the design of nonlocal metalenses, enabling highly efficient asymmetric wavefront shaping [39]. Furthermore, high-Q metasurfaces have found widespread applications in advanced terahertz devices, including terahertz biosensing and terahertz absorbers [40,41].

Historically, research has often focused separately on Fano resonances, QBIC resonances, and EIT phenomena [32,42,43]. However, synergies exist: EIT in photonic systems can be mimicked by coupling resonators or modes, typically a radiative bright mode and a subradiant dark mode. The bright mode couples directly to the incident light, while the dark mode is indirectly excited by the incident light through coupling effects—such as quantum coherence between atomic energy levels or near-field coupling in artificial structures. Destructive interference between the bright and dark modes induces the formation of a transparency window. QBICs, acting as exceptional dark modes, are ideally suited for opening EIT channels when coupled to a bright mode [44,45]. This coupling, mediated by symmetry breaking and interference, generates a pronounced transparency window. Furthermore, the inherently high Q-factor of the QBIC results in an extremely narrow resonance linewidth, significantly enhancing the EIT window's contrast and the system's sensitivity. This mechanism unlocks new avenues for designing high-performance photonic devices, including sensors and slow-light elements [19,25]. Crucially, integrating both QBIC resonance and the EIT effect within a single system promises enhanced functionalities, such as multi-band RI sensing and optical switching, beyond what is achievable with isolated resonances or EIT alone [46,47].

In this work, we propose a lithium niobate (LN) metasurface with tilted pyramid unit cells. Under y-polarized normal incidence, it simultaneously supports a SP-BIC resonance, manifested as a toroidal dipole (TD) resonance, and a pronounced EIT-like window in the 1500–1600 nm band. The EIT-like originates from a destructive interference between a super-radiant lattice mode (SLM) [48] and the high-Q QBIC mode derived from the symmetry-broken TD mode. The metasurface exhibits strong polarization-selective responses: only the SLM mode appears under x-polarization in 1500–1600 nm, while distinct SP-BIC modes arise in 1300–1400 nm (one mode for x-polarization, two modes for y-polarization). The EIT-related resonance achieves a RI sensitivity of 404.9 nm/RIU,

whereas the QBIC resonance reaches 887.7 nm/RIU. This design integrates multi-band BIC resonances and high-Q EIT in a single tunable platform, enabling advanced optical sensors. Compared with previously reported EIT-like or QBIC metasurfaces [44], our design eliminates the need for complex multilayer architectures [47] while maintaining resonance wavelengths that are nearly invariant with respect to the asymmetry parameter. This platform integrates multi-band BIC resonances and high-Q EIT effects within a single tunable configuration, offering significant advantages for advanced optical sensing. The pronounced polarization sensitivity of these high-Q resonances further enables polarization-controlled optical switching, where distinct QBIC modes can be selectively activated or suppressed by tuning the incident polarization state [49]. Additionally, the frequency-dependent response of such metasurfaces can be extended to space–time-coded designs, allowing for more versatile electromagnetic wave manipulation [50].

## 2. Structural Design and Methods

We use a specific design of all-dielectric metasurfaces, which comprise four LN pyramids in each unit cell, as shown in Figure 1. The corresponding lattice constant is denoted by P = 1800 nm. Each pyramid stands at a height of $H_1$ = 500 nm, with the lengths of its top and bottom edges measuring $L_1$ = 600 nm and $L_2$ = 900 nm, respectively. Supporting these pyramids is an LN plate, which has a thickness of $H_2$ = 140 nm at the base of each pyramid. The substrate chosen for the metasurface is silicon dioxide with a refractive index of 1.4 and a thickness of 500 nm. This type of ultrathin silicon dioxide substrate can be grown on p-type (100) silicon wafers through thermal oxidation [51] or alternatively prepared using methods such as reactive magnetron sputtering and selective chemical etching [52]. The structure exhibits mirror symmetry in the z-y plane while incorporating intentional symmetry breaking in the z-x plane through the centerward offset of pyramids along the *x*-axis, as seen in Figure 1b,c, transitioning from intrinsic $C_{4v}$ rotational symmetry (uniform inter-pyramid spacing $b_1$ in both directions when untilted) to an asymmetric configuration that achieves quasi-SP-BIC states by reducing the x-directional slit spacing to $b_2$, with the displacement parameter defined as $b = (b_1 - b_2)/2$. The LN pyramid metasurface structures can be fabricated through the following optimized procedure: a commercial LN film is first coated with a multilayer stack consisting of a thick resist, a chromium layer, and a second resist layer. The pattern is then defined using a variable-shaped beam electron writer, followed by sequential etching steps including reactive ion etching (RIE) for the chromium layer and reactive ion beam etching (RIBE) for the thick resist. Finally, the actual LN etching is performed via ion beam etching (IBE). This multi-step approach ensures both low sidewall roughness and high structural quality in the etched features [53,54]. The developed electric-field-driven nanoimprint technology enables the direct fabrication of large-area tilted metasurface nanostructures [55]. Numerous studies have utilized geometrically tilted structures to enhance the modulation capabilities of metasurfaces; for instance, tilted inverted pyramid structures have been employed to achieve efficient solar energy harvesting [56] and strong optical chirality [57]. Optical properties are simulated using COMSOL Multiphysics (v6.2) with Floquet–Bloch periodic boundary conditions applied to the x-z and y-z planes of the unit cell. The high Q-factors and pronounced field enhancement observed in BIC-based metasurfaces originate from collective modes sustained by their periodic lattice [58]. However, this inherent periodicity also renders the structures susceptible to finite sizes and edge effects. Since the formation of a well-defined quasi-BIC mode typically requires a minimum number of resonators (generally > 10 × 10) [59], the fabricated device dimensions must exceed this critical threshold to preserve the desired high-performance characteristics.

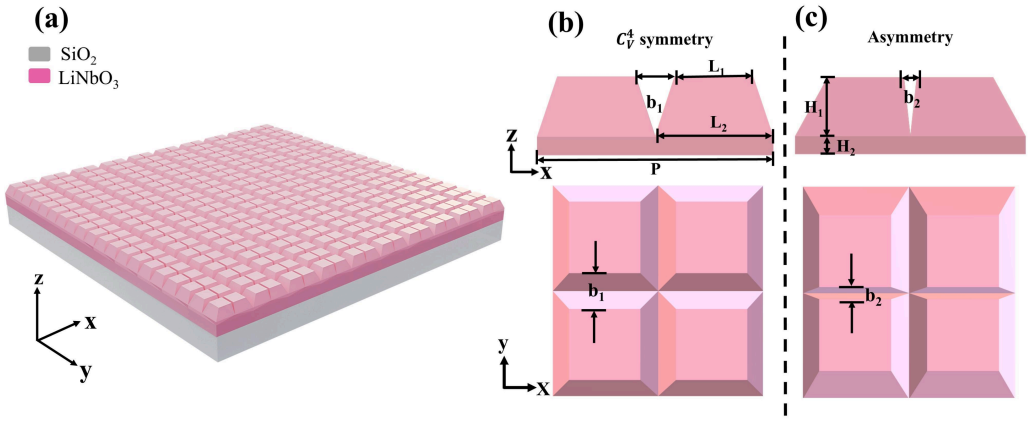



**Figure 1.** (**a**) Schematic of the multi-resonant metasurface featuring periodic LN pyramids. (**b**) Symmetric unit cell configuration with side and top views. (**c**) Asymmetric unit cell configuration with side and top views. The structure maintains a fixed period P = 1800 nm and has a pyramid geometry defined by top edge length $L_1$ = 600 nm, bottom edge length $L_2$ = 900 nm, and height $H_1$ = 500 nm, supported by a substrate layer of thickness $H_2$ = 140 nm. The thickness $H_3$ of the silicon dioxide substrate is 500 nm.

## 3. Excitation of Quais-SP-BIC and QBIC-EIT with Asymmetric Structures

We investigate the proposed pyramid-shaped LN metasurface by calculating its transmission spectra under different polarization states over a wide wavelength range from 1320 nm to 1580 nm. The results are shown in Figure 2a. The range from 1380 nm to 1500 nm is omitted due to the absence of strong resonance features requiring a comparison between symmetric and asymmetric metasurface designs. When pyramid tilts are absent along the *x*-axis, the structure exhibits $C_{4v}$ rotational symmetry, resulting in polarization-independent transmission, as presented by the black line in Figure 2a. It is clear that no resonance is observed within the 1320–1380 nm range, while a single broad-linewidth transmission dip appears in the 1500–1580 nm band, attributed to an SLM.

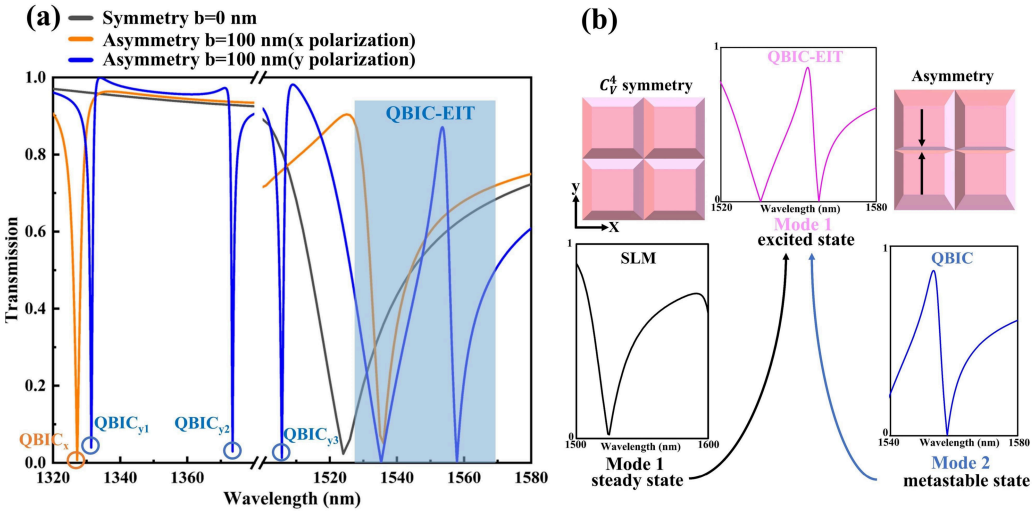



**Figure 2.** (**a**) The calculated transmission spectra for symmetric/asymmetric metasurface configurations under varied polarizations. The black line corresponds to the symmetric case. The orange line depicts x-polarized incidence on the asymmetric metasurface (b = 100 nm), marking the $QBIC_x$ mode (orange circle). The blue line represents y-polarized incidence on the asymmetric structure, indicating $QBIC_{y1/2/3}$ modes (blue circles). (**b**) Schematic of the formation of "QBIC-EIT" mode.

However, introducing a center-offset along the *x*-axis breaks the $C_{4v}$ rotational symmetry, rendering the metasurface polarization-dependent, as evidenced by the orange and black lines in Figure 2a. Consequently, this symmetry breaking transforms the ideal SP-BIC into a QBIC state, thus generating a narrow-linewidth transmission resonance. For example, under x-polarized normal incidence, as presented by the orange line in Figure 2a, a distinct resonance emerges in the 1300–1380 nm band, characteristic of a quasi-SP-BIC. We designate this resonance as $QBIC_x$ in Figure 2a. In contrast, the 1500–1580 nm band exhibits only the SLM, with no additional resonance features. Conversely, under y-polarized normal incidence, the asymmetric metasurface's transmission spectrum, as presented by the blue line in Figure 2a, exhibits two distinct resonances within 1300–1380 nm. These modes—labeled $QBIC_{y1}$ and $QBIC_{y2}$ via blue circles—similarly constitute quasi-symmetry-protected BICs.

Furthermore, under y-polarized illumination, the metasurface's transmission spectrum exhibits two additional resonances within the 1500–1580 nm band, which are at 1505 nm and 1555 nm, respectively, alongside the SLM. As shown by the blue line in Figure 2a, symmetry breaking induces a redshift in the SLM resonance. Critically, the QBIC mode at 1545 nm constructively interferes with the SLM, forming a novel "QBIC-EIT" hybrid mode [60]. This generation mechanism mirrors coherent interference in three-level atomic systems. Figure 2b shows the schematic diagram of the QBIC-EIT three-level Λ-type atomic system. In the photonic analogy of EIT, the system is modeled using Λ-shaped energy levels [10], comprising the ground state $|1\rangle$, excited state $|3\rangle$, and metastable state $|2\rangle$. The transition from $|1\rangle$ to $|3\rangle$ is mediated by an SLM mode with a high decay rate, which can be directly excited by y-polarized incident light. The transition from $|2\rangle$ to $|3\rangle$ is characterized by a BIC mode. When the pyramid is not tilted, its radiative decay rate is nearly zero, preventing direct coupling with freely propagating waves in free space. To achieve an observable transition, the pyramid is tilted here to convert the ideal BIC into a measurable QBIC mode. When y-polarized light is normally incident on the asymmetric metasurface structure, quantum interference occurs. The transition amplitudes from Mode 1 to Mode 3 and Mode 2 to Mode 3 undergo destructive interference, creating a narrow transparency window in the spectrum, termed the "QBIC-EIT" mode. It should be noted that this hybrid mode is an EIT-like mode rather than Autler–Townes Splitting (ATS). This is because ATS arises from the frequency splitting of two Lorentzian peaks and does not involve destructive interference [61]. In contrast, the QBIC-EIT mode is generated by the destructive interference between the bright SLM mode and the dark QBIC mode. The coupling strength g between the SLM and QBIC modes is quantified via coupled-mode theory as $g = \Delta\omega/2$, with strong coupling occurring when $g > \left|\gamma_{SLM} - \gamma_{QBIC}\right|/2$ [44]. The coupling is primarily mediated by near-field overlap rather than the radiation continuum, as confirmed by spatial overlap integrals κ. Symmetry breaking (pyramid tilt) increases κ by a factor of 2–3, directly enhancing the coupling strength.

## 4. Results and Discussion

### *4.1. CMT Theoretical Fitting and Q-Factor Analysis*

To model the SP-BIC resonance and its coupling with the SLM, we employ coupled mode theory (CMT). Within this framework, the transmission spectrum T($\omega$) is expressed as a function of angular frequency $\omega$ [62–64]:

$$T(\omega) = \frac{t^2(\omega - \omega_0)^2 + t^2 \cdot \gamma^2 + 2 \cdot r \cdot t(\omega - \omega_0) \cdot \gamma}{(\omega - \omega_0)^2 + \gamma^2} \quad (1)$$

where $\gamma$ is the total radiative attenuation rate, and $\omega_0$ is the frequency at the resonance peak, which can be obtained by calculating the eigenfrequency of the metasurface [18].

Here, $t$ and $r$ represent the transmission and reflection coefficients of the reference substrate spectra, respectively, obtained through electromagnetic simulation of the bare substrate structure [65,66]. We provide a detailed introduction to the derivation process of Equation (S1) in Supplementary Material Section S1. As shown in Figure 3a,b, our CMT fitting for all quasi-SP-BIC resonances demonstrates excellent agreement with COMSOL simulation results. Furthermore, we model the interaction between the low-Q SLM mode and the high-Q BIC mode, mirroring the EIT effect in three-level atomic systems. The transparency window originates from SLM-QBIC mode coupling during QBIC-EIT resonance. For our CMT analysis, we simplify the coupling equations by excluding intermodal interactions. As shown in Figure 3c, the fitted transmission spectrum demonstrates close agreement with COMSOL simulations, with minor deviations attributable to neglected mode couplings [1,67].

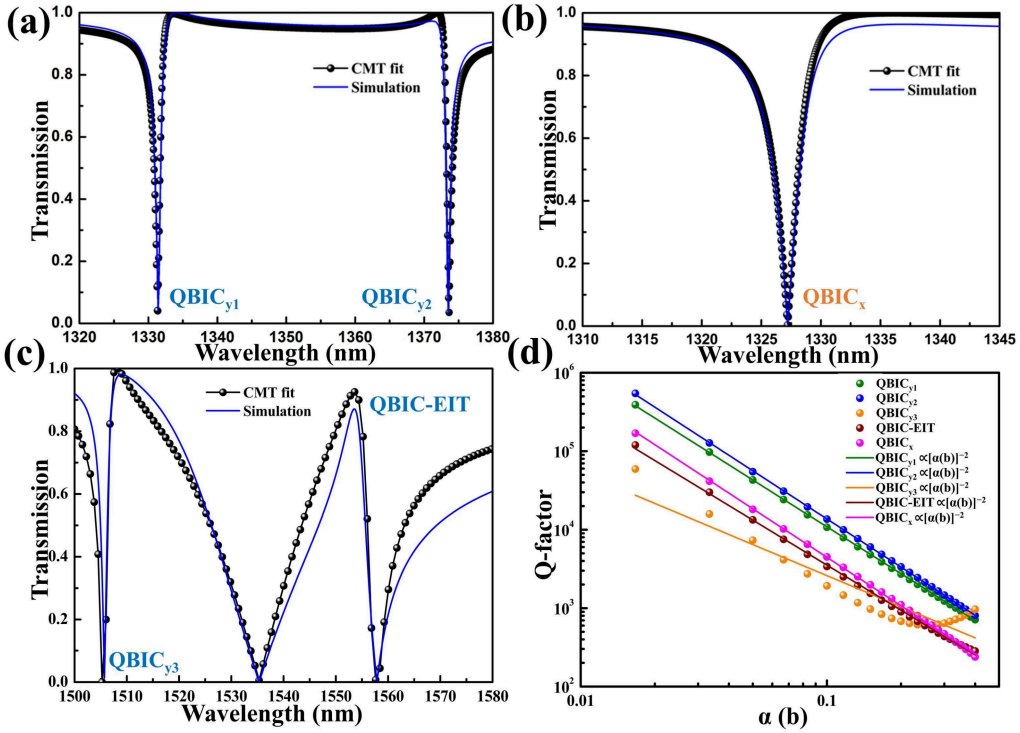



**Figure 3.** CMT analysis of QBIC and QBIC-EIT modes: (**a**) QBIC$_{y1}$ and QBIC$_{y2}$ mode comparisons between CMT fitting curves (dotted black lines) and simulated transmission spectra (solid blue lines). (**b**) Equivalent validation for QBIC$_x$ mode, demonstrating agreement between theoretical fits and computational results. (**c**) Concurrent analysis for QBIC$_{y3}$ and QBIC-EIT modes, highlighting modal coupling dynamics. (**d**) Q-factor evolution across resonant modes as a function of asymmetry parameter, $a$(b), illustrating divergent behavior at minimal offsets.

Using the CMT, we extract the Q-factors of individual modes through the relationship $Q = \omega_0/2\gamma$ [68,69], where $\omega_0$ is the resonance frequency (real part of the complex eigenfrequency) and $\gamma$ is the leakage rate (imaginary part of the eigenfrequency). An appealing feature of quasi-BIC metasurfaces is their capacity to tailor the Q-factor and radiation properties through structural parameter tuning. We define the asymmetry parameter associated with the pyramid displacement as $a(b) = b/b_1$, where $b_1$ denotes the slit spacing between pyramids under perfect symmetry. The Q-factors of the respective modes are plotted against the asymmetry parameter $a(b)$ in Figure 4d. Evidently, the Q-factor is proportional to the inverse square of the asymmetry parameter, $a(b)$. As b decreases, all Q-factors increase monotonically, diverging to infinity as $b \to 0$. This asymptotic behavior confirms all five modes as symmetry-protected SP-BICs [36]. The dependence of the Q-factor of the

$QBIC_{y3}$ mode on the asymmetry parameter deviates from the simple inverse-square law. This is mainly because a QBIC mode typically manifests as the scattering enhancement of a single dipole accompanied by the suppression of other dipoles in the multipole decomposition [70]. In contrast, the multipole decomposition of the $QBIC_{y3}$ mode reveals a hybrid of TD and MD. The coexistence and interaction of different multipole moments affect the overall radiation rate. A detailed multipole analysis of the QBICs will be presented in the next section. A smaller asymmetry parameter yields a higher Q-factor. The resulting higher Q-factor leads to a narrower resonance linewidth, which, according to the standard definition of the FOM, directly enhances the sensor's performance. Furthermore, we analyze the eigenfrequency components of all modes versus the offset parameter $b$. As shown in Figure S1, the total radiative attenuation rate, as presented with the red dotted line, increases with $b$, consistent with Q-factor calculations, while the eigenfrequency real component, as presented with the black dotted line, remains virtually unaffected by $b$. Resonance positions exhibit minimal shift with varying $b$, confirming exceptional spectral stability in the metasurface design despite fabrication tolerances. Furthermore, we introduced rounded corners and sidewall roughness to the metasurface unit cells and compared the Q-factors of all resonant modes before and after the roughness treatment, as shown in Figure S2. The results demonstrate that, despite the introduced roughness, most QBIC resonances and QBIC-EIT modes maintain their Q-factors without significant degradation, except for the $QBIC_x$ resonance, which shows a relatively noticeable reduction. This indicates that these QBIC resonances and QBIC-EIT modes possess relatively stable performance against fabrication imperfections. The resonance quality of high-Q structures can be affected by the finite linewidth of the excitation source. One method to evaluate the structure's response to a beam of finite width is to examine its angular dependence [49]. We calculated the transmission spectra of $QBIC_x$, $QBIC_{y1}$, and $QBIC_{y2}$ under incident angles ranging from 0° to 2°, as shown in Figure S3 in the Supplementary Material. All these QBIC resonances exhibit a redshift that increases with the incident angle. Nevertheless, the resonances do not vanish, and their linewidths remain stable, indicating that the designed structure exhibits a certain robustness to angular deviations. Since the numerical aperture (NA) of a probe beam directly defines its angular spread ($NA = n\sin\theta_{max}$), the demonstrated robustness of the QBIC resonances over a 0–2° incident angle range (corresponding to $NA \approx 0.035$ in air) confirms that the platform is resilient to the typical angular divergence encountered in practical implementations with moderate-NA probe beams.

### *4.2. Multipole Expansion and Electromagnetic Field Analysis of Resonant Modes*

To further elucidate this EIT-like and QBIC dual-resonance system, we simulated the electric and magnetic field profiles and performed a Cartesian multipole decomposition of the far-field scattering cross section near the resonance wavelengths [71,72]. The detailed methodology for multipole decomposition is provided in Supplementary Material Section S4. Figure 4 presents the multipole expansion analysis for the four resonances under y-polarized illumination, with scattering radiation intensities normalized for comparison. As clearly shown, these modes are predominantly governed by TD and magnetic dipole (MD) contributions. The insets in Figure 4 depict the magnetic field z-components and corresponding surface current distributions for each mode. Specifically, the $QBIC_{y1}$ mode in Figure 4a exhibits concentrated magnetic field z-components at the pyramid centers, displaying dipolar patterns symmetric along the *y*-axis. Surface currents form circulating loops on both the top surfaces and sidewalls of each pyramid. Crucially, coupled circulating currents among the four pyramids collaboratively form a TD moment—a characteristic TD signature consistent with the multipole decomposition results.

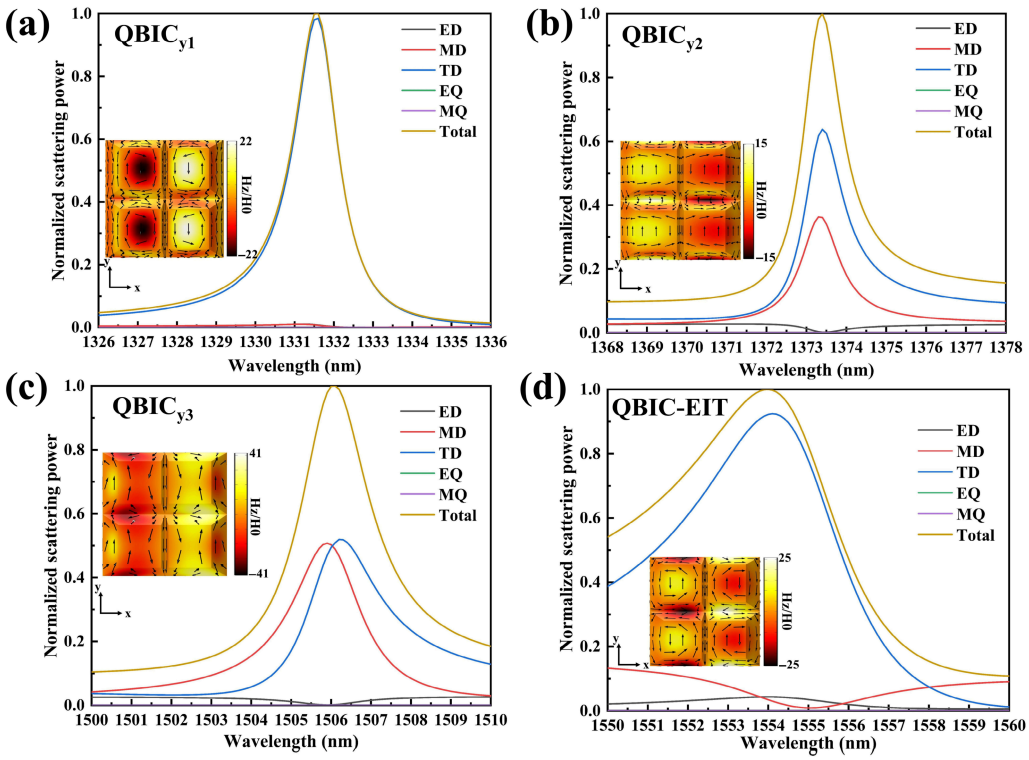



**Figure 4.** The multipole decomposition analysis of the four resonant modes under y-polarized illumination, plotting normalized far-field scattering intensities: (**a**) The QBIC$_{y1}$ mode is dominated by the TD. (**b**) QBIC$_{y2}$ features joint contributions from the TD and MD. (**c**) QBIC$_{y3}$ similarly exhibits co-dominant TD and MD characteristics. (**d**) The QBIC-EIT mode displays predominant TD excitation. Insets show the corresponding magnetic field distributions, with black arrows indicating surface current density vectors.

Similarly, the QBIC$_{y2}$ mode in Figure 4b also arises from the TD excitation. Its maximum magnetic field z-component localizes on the pyramid sidewalls oriented along the *x*-axis. Interconnected circulating currents between adjacent sidewalls establish a clear TD configuration. Concurrently, weaker magnetic field components at the pyramid centers, accompanied by sparse *x*-axis-oriented circulating currents, suggest reduced MD activity. It is interesting to note that the QBIC$_{x}$ mode also exhibits strong TD character (see Figure S4 in the Supplementary Material). Here, the magnetic field z-component primarily concentrates on the pyramids' upper surfaces, with surface currents forming circulating loops. However, although both the QBIC$_{y1}$ and QBIC$_{x}$ modes in the same spectral band are dominated by the TD response, their magnetic field distributions exhibit distinct characteristics due to different incident polarizations: the bright and dark mode distributions of QBIC$_{y1}$ are symmetric about the *y*-axis, while those of QBIC$_{x}$ are symmetric about the *x*-axis, directly corresponding to their respective excitation polarizations. This indicates that the polarization dependence induced by the geometric asymmetry of the structure also influences the polarization behavior of the TD.

In contrast, the QBIC$_{y3}$ mode arises from the combined action of MD and TD components. The inset in Figure 4c reveals an elliptical distribution of the magnetic field z-component concentrated on x-oriented sidewalls, resembling the QBIC$_{y2}$ mode. Here, sidewall current coupling generates toroidal moments. Distinctively, this mode simultaneously exhibits enhanced magnetic field components and corresponding circulating currents on y-oriented sidewalls, manifesting concurrent MD characteristics. This combination mechanism, quantitatively verified by multipole decomposition, shows close agreement with the observed electromagnetic field distributions.

We perform the multipole analysis of the QBIC-EIT hybrid mode, which reveals distinct operational regimes. The SLM mode near 1540 nm in Figure S5 of the Supplementary Material shows predominant MD, TD, and electric dipole (ED) contributions. Notably, despite symmetry breaking, its far-field scattering maintains displacement-independent flat spectral responses rather than resonant behavior. Concurrently, the QBIC resonance at 1554 nm, as shown in Figure 4d, demonstrates TD-dominated characteristics, namely toroidally coupled current loops bridging pyramid tops and *y*-axis sidewalls generate collective TD moments, while z-component magnetic field concentrations at geometric centers and sidewall junctions validate the toroidal excitation mechanism through multipole decomposition consistency. When symmetry is broken, the TD mode becomes dominant and suppresses the far-field scattering of other dipoles. The BIC mode near the SLM mode undergoes radiative leakage and transforms into a QBIC, resulting in an asymmetric Fano resonance peak in the transmission spectrum. As the asymmetry parameter b gradually increases, the SLM undergoes a frequency shift and approaches the QBIC located at 1554 nm, coupling with it to form a new QBIC-EIT mode.

### *4.3. Enhanced RI Sensitivity with the Asymmetric Metasurface*

The EIT-like window and QBIC resonance offer exceptional potential for high-sensitivity RI sensing due to their sharp, high-Q resonance. High-Q resonance implies that the field is largely confined within the structure, resulting in minimal outward radiative scattering loss. This enables a narrower linewidth, which in turn improves the achievable detection limit and FOM [49]. Despite this internal confinement, the evanescent tail extends 80–150 nm into the analyte (the $1/e$ penetration depth), ensuring practical accessibility for surface-bound molecules. Figure 5 demonstrates the excellent sensitivity of our dual-resonance metasurface design. The refractive index variation range for most gases falls within 1.0–1.1, whereas the refractive index range for most liquids lies between 1.3 and 1.5 [49]. To evaluate its sensing capability, we placed the metasurface in a 3 μm high gas cell during simulations and varied the background refractive index n from 1.00 to 1.05 in increments of 0.01 to emulate a gaseous environment. Under y-polarized illumination with offset b = 100 nm, even minute changes in RI induce significant redshifts in both the SP-$BIC_{y3}$ resonance and EIT-like window positions, as shown in Figure 5a. To quantify the metasurface's sensing capability, we define sensitivity S as the spectral shift per RI unit (RIU), i.e., $S = \Delta\lambda/\Delta n$. Figure 5b shows the linear fitting curves for the $QBIC_{y3}$ and QBIC-EIT resonance. The sensitivities are $S_{QBICy3}$ = 422.0 nm/RIU and $S_{QBIC\text{-}EIT}$ = 404.9 nm/RIU. Another key sensing metric is FOM, defined as FOM = S/FWHM, where FWHM is the full width at half maximum of the transmission peak. This definition is rigorously valid for Lorentzian resonances. However, for EIT-like or Fano profiles that exhibit asymmetry, the FWHM still provides a practically useful measure of spectral sharpness and resolving power, albeit as an approximation. The widespread use of this metric in EIT, QBIC, and Fano resonance sensing literature [18,73] enables consistent cross-platform comparison, and we adopt it here for that purpose. When precise line-shape fitting is required, an alternative metric such as $FOM^* = S/FWHM_{eff}$ based on an asymmetric line-shape model could be employed, but this lies beyond the scope of the present work. The $QBIC_{y3}$ resonance (FWHM = 1 nm) yields FOM = 422.0 $RIU^{-1}$. The wider QBIC-EIT window (FWHM = 2.5 nm) achieves FOM = 162 $RIU^{-1}$. We also investigated the $QBIC_{y1}$ and $QBIC_{y2}$ modes, as shown in Figure S6 in the Supplementary Material. These two resonant modes exhibit relatively lower sensitivity to environmental refractive index changes, with $QBIC_{y1}$ demonstrating a sensitivity of S = 866.0 nm/RIU and $QBIC_{y2}$ achieving S = 218.9 nm/RIU. Despite its lower sensitivity, $QBIC_{y2}$'s exceptionally narrow linewidth (FWHM = 0.8 nm) results in a higher FOM.

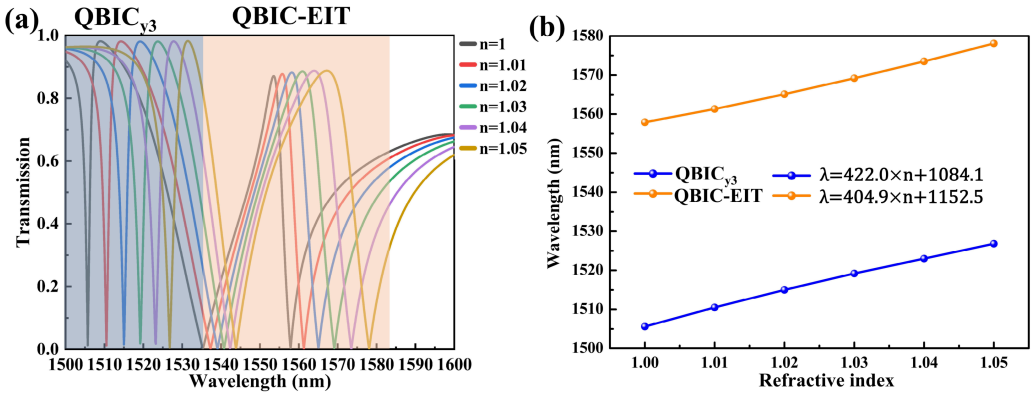



**Figure 5.** RI sensing of QBIC$_{y3}$ and QBIC-EIT modes: (**a**) Evolution of transmission spectra for the QBIC$_{y3}$ mode (blue-highlighted window) and QBIC-EIT resonance (orange-highlighted window) under varying ambient refractive indices. (**b**) QBIC$_{y3}$ dip shift tracking (blue dotted-line markers) and QBIC-EIT peak shift monitoring (orange dotted-line markers).

Additionally, the QBIC$_x$ resonance induced in the 1300 nm band under x-polarized illumination exhibits ultra-high RI sensing sensitivity. As shown in Figure 6a, the QBIC$_x$ resonance undergoes significant redshifting with minimal changes in RI ($\Delta n = 0.1$). Its linear fitting curve in Figure 6b yields an RI sensitivity of S = 887.7 nm/RIU, with FWHM = 1 nm and FOM = 887.7 RIU$^{-1}$. Intriguingly, the sensitivity remains largely unaffected as structural offset b decreases. With diminishing b, the metasurface's symmetry breaking becomes increasingly subtle, causing the QBIC's Q-factor to approach the theoretically infinite Q of a true BIC. This corresponds to a reduced radiative lifetime and a narrower resonance linewidth. At b = 50 nm, FWHM = 0.6 nm, and at b = 10 nm, FWHM = 0.1 nm. While reducing b does not enhance RI sensitivity directly, the metasurface's sensing FOM improves dramatically due to the sharp decrease in linewidth. Specifically, FOM reaches 1497.3 RIU$^{-1}$ at b = 50 nm and 9014 RIU$^{-1}$ at b = 10 nm. This designed metasurface enables dual-band, multi-resonance RI sensing with exceptional sensitivity and FOM across polarizations, demonstrating strong potential as a highly efficient RI sensor.

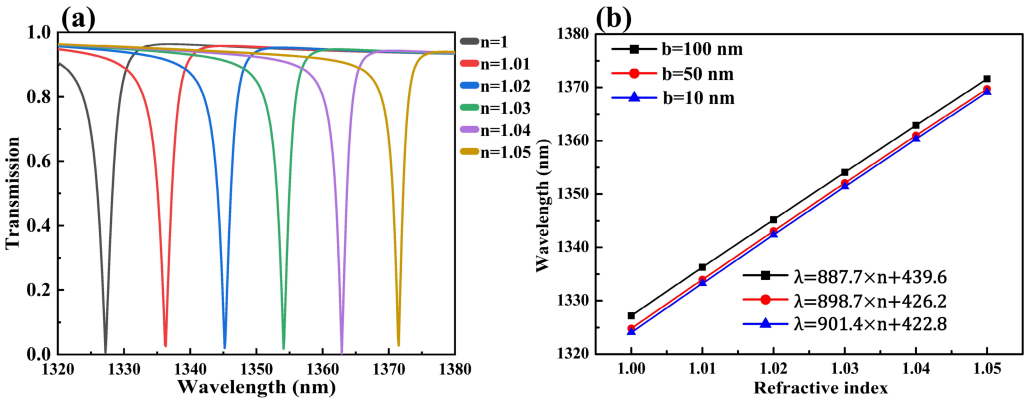



**Figure 6.** Refractometric sensing and displacement-dependent sensitivity analysis of the QBIC$_x$ Mode: (**a**) Evolution of the QBIC$_x$ transmission spectra with surrounding RI. (**b**) Sensitivity calibration plots for QBIC$_x$ at different displacement parameters b, showing linear regression fits of resonance wavelength versus RI.

Our designed metasurface structure demonstrates applicability for sensing in high-refractive-index liquid environments. In our simulations, a 500 nm thick analyte layer was applied to the metasurface, with the analyte's refractive index varied from 1.3 to 1.5 in steps of 0.05. The corresponding sensing performance of the QBIC$_{y1}$, QBIC$_{y2}$, and QBIC$_x$

modes is shown in Figure S7. In high-refractive-index environments, the refractive index sensitivity of $QBIC_x$, $QBIC_{y1}$, and $QBIC_{y2}$ is considerably lower than that in low-refractive-index gas environments. This reduction occurs because the high-refractive-index liquid increases the asymmetry in the dielectric environment, thereby broadening the resonance linewidth and consequently degrading the sensing performance [74]. Furthermore, the existing literature also indicates that the sensing performance of all-dielectric metasurfaces in high-refractive-index liquids is generally inferior to their performance in low-refractive-index gas detection [75]. Our results align with this established trend. The calculated sensitivities are 190 nm/RIU for $QBIC_{y1}$, 135 nm/RIU for $QBIC_{y2}$, and 138.2 nm/RIU for $QBIC_x$. Although these values are lower than those in gaseous environments due to reduced field confinement contrast, they remain competitive. For instance, our sensitivities are still higher than those reported for a silicon-based superstructure operating in the same detection wavelength band [76].

Furthermore, as shown in Figure S7d, we analyzed the effect of analyte thickness on the metasurface's sensing performance. When the analyte thickness was increased from 250 nm to 1000 nm, the refractive index sensitivity exhibited only minimal variation. This indicates that the analyte thickness has an insignificant impact on the refractive index sensitivity, highlighting a favorable characteristic for practical device fabrication and measurement scenarios. Previous studies suggest that incorporating two-dimensional materials (such as perovskites) onto the metasurface could enhance aqueous solution sensing performance due to their excellent stability and water molecule adsorption properties [77]. In summary, although the refractive index sensing performance is reduced in high-refractive-index environments, our structure remains suitable for sensing applications under such conditions.

We compared the sensing performance of our designed device with recent metasurface-based sensors in the infrared regime, as summarized in Table 1. It is worth noting that conventional single-resonance sensing may suffer from inaccuracy and unreliability due to spectral shifts induced by environmental fluctuations in temperature, humidity, and intrinsic instrumental drift. This limitation can be effectively mitigated by transitioning from single- to dual-resonance sensing strategies, where the dependence of resonance wavelengths on the ambient refractive index can be well described by first-order perturbation theory [78]. A broader comparison with representative metasurface sensors is provided. The anapole-mode-based Si elliptical metasurface [79] supports only a single resonance and exhibits lower sensitivity and FOM in gaseous environments than our platform. The all-dielectric a-Si dual-resonance metasurface [76] shows high sensitivity in liquid environments but has an FOM of only 66, which is substantially lower than that of our work. Conversely, a dual-resonance gold plasmonic metasurface [80] achieves a narrower FWHM in high-refractive-index environments, resulting in a relatively high FOM; however, its refractive index sensitivity is lower than that achieved in our platform. Polarization-selective quasi-BIC resonances have been reported in other all-dielectric metasurfaces [81]. In comparison, our LN-based tilted pyramid platform simultaneously supports three independent high-Q resonances with polarization control and exhibits resonance robustness against asymmetry variations—advantages not demonstrated in [81]. While most prior works have focused on either single- or dual-resonance schemes, our metasurface supports multiple resonances across different wavelength bands and exhibits strong polarization dependence, offering distinct advantages for broadband detection. Although the FOM of our sensor is moderate compared to other works, the maximum sensitivity of 887.7 nm/RIU achieved here surpasses that of many recently reported metasurface sensors. Such high sensitivity is particularly advantageous in gas sensing applications, where minute refractive index changes need to be detected.

**Table 1.** Performance comparison of refractive index sensors in the near-infrared region.

| Year | Structure | Resonance Mode | Maximum Sensitivity (nm/RIU) | FOM | Polarization Dependence | Resonance Number | Detection Range |
|---|---|---|---|---|---|---|---|
| This work | LN pyramid | QBIC&EIT-like | 887.7 | 887.7 | yes | 5 | 1–1.05<br>1.3–1.5 |
| 2025 [73] | Dielectric Dumbbell hole | QBIC&anapole | 745 | 1650 | yes | 2 | 1–1.04<br>1.3–1.5 |
| 2023 [78] | Si cylindroid | QBIC | 122.2 | 206.1 | no | 2 | 1–1.5 |
| 2023 [80] | Gold plasma film | SPP-SLR | 514 | 1431 | no | 2 | 1–1.384 |
| 2025 [76] | Amorphous Si column | QBIC | 413 | 66 | no | 2 | 1.3–1.6 |
| 2025 [79] | Si cylindroid with hole | anapole | 393.4 | 596.1 | no | 1 | 1–1.05 |
| 2026 [81] | GaP bow-tie-shaped nanoholes | QBIC | 342 | 217.1 | yes | 4 | 1.3–1.4 |

## 5. Conclusions

In summary, we theoretically designed a dielectric metasurface that supports multiple SP-BICs and a QBIC-EIT hybrid mode. Enabled by a periodic array of displaced LN pyramids, the structure exhibits distinct resonant behaviors under different polarization states and across separate wavelength bands. Through systematic analysis using CMT and multipole decomposition, we clarified that these resonances originate from either pure TD excitations or hybridized TD–MD interactions. The proposed metasurface demonstrates exceptional RI sensing performance, with sensitivities as high as 887.7 nm/RIU and 866.0 nm/RIU for the $QBIC_x$ and $QBIC_{y1}$ modes, respectively, and 422.0 nm/RIU and 404.9 nm/RIU for the $QBIC_{y3}$ and QBIC-EIT modes. Importantly, the resonance frequencies show minimal dependence on the geometric displacement parameter $b$, ensuring strong fabrication tolerance—significant structural deviations introduce only negligible spectral shifts and no appreciable degradation in sensitivity. This work not only advances the practical implementation of high-performance refractive index sensing metasurfaces but also enables multi-band, high-sensitivity detection, offering a novel technical pathway for applications such as gas refractive index monitoring.

**Supplementary Materials:** The following supporting information can be downloaded at: https://www.mdpi.com/article/10.3390/s26092632/s1, Section S1: Coupled-mode theory for QBICs and QBIC-EIT; Table S1: Fitting parameters for the five modes in CMT analysis; Figure S1: Real and imaginary parts of the eigenfrequencies for each mode as a function of the offset parameter b; Section S2: Q-factor degradation analysis due to fabrication roughness; Figure S2: Q-factor degradation analysis due to fabrication roughness; Figure S3: Analysis of QBIC Mode Stability under Angular Variation; Section S3: Multipole expansion and scatting power; Figure S4: Multipole decomposition of the $QBIC_x$ mode; Figure S5: Multipole decomposition of the SLM mode; Section S4: Further Analysis on the Sensitivity of Refractive Index Sensing; Figure S6: The refractive index sensing of $QBIC_{y1}$ and $QBIC_{y2}$; Figure S7. Liquid high-refractive-index sensing and resonance-wavelength-based sensitivity analysis of $QBIC_{y1}$, $QBIC_{y2}$, and $QBIC_x$ modes.

**Author Contributions:** C.Z.: writing—original draft preparation and data curation; W.Z.: visualization; J.L.: formal analysis; J.C.: software; Y.S.: funding acquisition and project administration; L.H.: investigation and writing—review; T.G.: writing—review and editing and methodology. All authors have read and agreed to the published version of the manuscript.

**Funding:** This work was supported by the National Natural Science Foundation of China (12104203, 12464057, and 12264027); the Jiangxi Provincial Natural Science Foundation (20242BAB25039, 20224BAB211015, 20242BAB20024, and 20252BAC240067); and the Double Thousand Plan of Jiangxi Province (No. jxsq2023101069).

**Institutional Review Board Statement:** Not applicable.

**Informed Consent Statement:** Not applicable.

**Data Availability Statement:** The data presented in this study are available on request from the corresponding authors.

**Conflicts of Interest:** The authors declare no conflict of interest.

## Abbreviations

The following abbreviations are used in this manuscript:

| | |
|---|---|
| BIC | Bound states in the continuum |
| EIT | Electromagnetically induced transparency |
| RI | Refractive index |
| S | Sensitivity |
| FOM | Figure of merit |

## References


1. Yu, J.; Yao, W.; Qiu, M.; Li, Q. Free-space high-Q nanophotonics. *Light Sci. Appl.* **2025**, *14*, 174. [CrossRef] [PubMed]
2. Eisaman, M.D.; André, A.; Massou, F.; Fleischhauer, M.; Zibrov, A.S.; Lukin, M.D. Electromagnetically induced transparency with tunable single-photon pulses. *Nature* **2005**, *438*, 837–841. [CrossRef] [PubMed]
3. Fleischhauer, M.; Imamoglu, A.; Marangos, J.P. Electromagnetically induced transparency: Optics in coherent media. *Rev. Mod. Phys.* **2005**, *77*, 633–673. [CrossRef]
4. Harris, S.E.; Field, J.E.; Imamoğlu, A. Nonlinear optical processes using electromagnetically induced transparency. *Phys. Rev. Lett.* **1990**, *64*, 1107–1110. [CrossRef]
5. Ham, B.S.; Hemmer, P.R.; Shahriar, M.S. Efficient electromagnetically induced transparency in a rare-earth doped crystal. *Opt. Commun.* **1997**, *144*, 227–230. [CrossRef]
6. Bhattarai, M.; Bharti, V.; Natarajan, V.; Sargsyan, A.; Sarkisyan, D. Study of EIT resonances in an anti-relaxation coated Rb vapor cell. *Phys. Lett. A* **2019**, *383*, 91–96. [CrossRef]
7. Joshi, A.; Xiao, M. Optical Multistability in Three-Level Atoms inside an Optical Ring Cavity. *Phys. Rev. Lett.* **2003**, *91*, 143904. [CrossRef]
8. Autler, S.H.; Townes, C.H. Stark Effect in Rapidly Varying Fields. *Phys. Rev.* **1955**, *100*, 703–722. [CrossRef]
9. Liu, N.; Mesch, M.; Weiss, T.; Hentschel, M.; Giessen, H. Infrared Perfect Absorber and Its Application As Plasmonic Sensor. *Nano Lett.* **2010**, *10*, 2342–2348. [CrossRef] [PubMed]
10. Hamedi, H.R.; Ruseckas, J.; Juzeliūnas, G. Electromagnetically induced transparency and nonlinear pulse propagation in a combined tripod and Λ atom-light coupling scheme. *J. Phys. B At. Mol. Opt. Phys.* **2017**, *50*, 185401. [CrossRef]
11. Zeng, A.W.; Guo, B. Characteristics of slow light in a magnetized plasma hyperbolic metamaterial waveguide. *Opt. Quantum Electron.* **2017**, *49*, 200. [CrossRef]
12. Serapiglia, G.B.; Paspalakis, E.; Sirtori, C.; Vodopyanov, K.L.; Phillips, C.C. Laser-Induced Quantum Coherence in a Semiconductor Quantum Well. *Phys. Rev. Lett.* **2000**, *84*, 1019–1022. [CrossRef] [PubMed]
13. Joshi, A.; Brown, A.; Wang, H.; Xiao, M. Controlling optical bistability in a three-level atomic system. *Phys. Rev. A* **2003**, *67*, 041801. [CrossRef]
14. Satpathy, S.; Roy, A.; Mohapatra, A. Fano interference in classical oscillators. *Eur. J. Phys.* **2012**, *33*, 863. [CrossRef]
15. Souza, J.A.; Cabral, L.; Oliveira, R.R.; Villas-Boas, C.J. Electromagnetically-induced-transparency-related phenomena and their mechanical analogs. *Phys. Rev. A* **2015**, *92*, 023818. [CrossRef]
16. Xiao, S.; Wang, T.; Liu, T.; Yan, X.; Li, Z.; Xu, C. Active modulation of electromagnetically induced transparency analogue in terahertz hybrid metal-graphene metamaterials. *Carbon* **2018**, *126*, 271–278. [CrossRef]
17. Safavi-Naeini, A.H.; Alegre, T.P.M.; Chan, J.; Eichenfield, M.; Winger, M.; Lin, Q.; Hill, J.T.; Chang, D.E.; Painter, O. Electromagnetically induced transparency and slow light with optomechanics. *Nature* **2011**, *472*, 69–73. [CrossRef]
18. Yang, Y.; Kravchenko, I.I.; Briggs, D.P.; Valentine, J. All-dielectric metasurface analogue of electromagnetically induced transparency. *Nat. Commun.* **2014**, *5*, 5753. [CrossRef]
19. Liu, H.; Zhao, J.; Chen, C.; Gao, P.; Dai, Y.; Lu, X.; Wan, Y.; Zhao, S.; Wang, X. Switchable multifunctional metasurface based on electromagnetically induced transparency and photosensitive silicon. *Opt. Quantum Electron.* **2023**, *56*, 176. [CrossRef]
20. Su, H.; Wang, H.; Zhao, H.; Xue, T.; Zhang, J. Liquid-Crystal-Based Electrically Tuned Electromagnetically Induced Transparency Metasurface Switch. *Sci. Rep.* **2017**, *7*, 17378. [CrossRef]

21. Yuan, T.; Bo, Y.; Wu, J.; Du, Y. Terahertz Meta-surface Sensor with Various Refractive Indexes Based on EIT-like Effect. In *Proceedings of the 2022 47th International Conference on Infrared, Millimeter and Terahertz Waves (IRMMW-THz), Delft, The Netherlands, 28 August–2 September 2022*; IEEE: New York, NY, USA, 2022; pp. 1–2.
22. Ma, T.; Huang, Q.; He, H.; Zhao, Y.; Lin, X.; Lu, Y. All-dielectric metamaterial analogue of electromagnetically induced transparency and its sensing application in terahertz range. *Opt. Express* **2019**, *27*, 16624–16634. [CrossRef]
23. Wang, L.; Gao, Z.; Hou, Z.; Song, J.; Liu, X.; Zhang, Y.; Wang, X.; Yang, F.; Shi, Y. Active Modulation of an All-Dielectric Metasurface Analogue of Electromagnetically Induced Transparency in Terahertz. *ACS Omega* **2021**, *6*, 4480–4484. [CrossRef]
24. Khan, H.A.; Shah, S.W.; Khan, A.D. Electromagnetic-Induced Transparency and Slow Light in Plasmonic Metasurfaces. *Plasmonics* **2022**, *17*, 51–58. [CrossRef]
25. Zhao, X.; Huang, R.; Du, X.; Zhang, Z.; Li, G. Ultrahigh-Q Metasurface Transparency Band Induced by Collective–Collective Coupling. *Nano Lett.* **2024**, *24*, 1238–1245. [CrossRef] [PubMed]
26. Nakanishi, T.; Kitano, M. Storage and retrieval of electromagnetic waves using electromagnetically induced transparency in a nonlinear metamaterial. *Appl. Phys. Lett.* **2018**, *112*, 201905. [CrossRef]
27. Yang, J.; Wang, T.; Fang, G.; Qi, L.; Chen, X. Chiral identification of lactic acid enantiomers by an achiral terahertz metasurface sensor. *Opt. Laser Technol.* **2024**, *172*, 110487. [CrossRef]
28. Zhao, J.; Zhang, L.; Liang, H. Advances in Metasurface-Based Terahertz Sensing. *Adv. Phys. Res.* **2024**, *3*, 2400077. [CrossRef]
29. Wang, B.-X.; Duan, G.; Lv, W.; Tao, Y.; Xiong, H.; Zhang, D.-Q.; Yang, G.; Shu, F.-Z. Design and experimental realization of triple-band electromagnetically induced transparency terahertz metamaterials employing two big-bright modes for sensing applications. *Nanoscale* **2023**, *15*, 18435–18446. [CrossRef]
30. Hsu, C.W.; Zhen, B.; Stone, A.D.; Joannopoulos, J.D.; Soljačić, M. Bound states in the continuum. *Nat. Rev. Mater.* **2016**, *1*, 16048. [CrossRef]
31. Marinica, D.C.; Borisov, A.G.; Shabanov, S.V. Bound States in the Continuum in Photonics. *Phys. Rev. Lett.* **2008**, *100*, 183902. [CrossRef] [PubMed]
32. Azzam, S.I.; Kildishev, A.V. Photonic Bound States in the Continuum: From Basics to Applications. *Adv. Opt. Mater.* **2021**, *9*, 2001469. [CrossRef]
33. Neale, S.; Muljarov, E.A. Accidental and symmetry-protected bound states in the continuum in a photonic-crystal slab: A resonant-state expansion study. *Phys. Rev. B* **2021**, *103*, 155112. [CrossRef]
34. Sadrieva, Z.F.; Belyakov, M.A.; Balezin, M.A.; Kapitanova, P.V.; Nenasheva, E.A.; Sadreev, A.F.; Bogdanov, A.A. Experimental observation of a symmetry-protected bound state in the continuum in a chain of dielectric disks. *Phys. Rev. A* **2019**, *99*, 053804. [CrossRef]
35. Friedrich, H.; Wintgen, D. Physical realization of bound states in the continuum. *Phys. Rev. A* **1985**, *31*, 3964–3966. [CrossRef] [PubMed]
36. Koshelev, K.; Lepeshov, S.; Liu, M.; Bogdanov, A.; Kivshar, Y. Asymmetric Metasurfaces with High-Q Resonances Governed by Bound States in the Continuum. *Phys. Rev. Lett.* **2018**, *121*, 193903. [CrossRef]
37. Zhou, W.; Sun, G.; Yuan, Y.; Wang, Y.; Burokur, S.N.; Wang, Y.; Zhang, K. Bound States in the Continuum in Photonics and Metasurfaces: From Phenomena to Applications. *Ann. Der Phys.* **2025**, *537*, 2400250. [CrossRef]
38. Gao, X.; Hsu, C.W.; Zhen, B.; Lin, X.; Joannopoulos, J.D.; Soljačić, M.; Chen, H. Formation mechanism of guided resonances and bound states in the continuum in photonic crystal slabs. *Sci. Rep.* **2016**, *6*, 31908. [CrossRef]
39. Yao, J.; Wang, Z.; Fan, Y.; Zhang, K.; Lin, R.; Wu, J.; Peng, C.; Xiao, S.; Tsai, D.P. Intensity-asymmetric wavefront shaping in nonlocal meta-lens. *Nat. Commun.* **2026**, *17*, 2039. [CrossRef]
40. Zhou, X.; Li, L.; Shen, Y.; Hong, L.; Lin, D.; Guo, T.; Lei, J. Design, simulation, and experimental realization of a high-sensitivity polarization-independent electromagnetically induced transparent terahertz metamaterials. *Opt. Express* **2024**, *32*, 33130–33143. [CrossRef]
41. Chou Chau, Y.-F. Enhancing broadband terahertz absorption via a graphene-based metasurface absorber featuring a rectangular ring and triple crossbars. *Phys. Scr.* **2024**, *99*, 055905. [CrossRef]
42. Yan, C.; Yang, K.-Y.; Martin, O.J.F. Fano-resonance-assisted metasurface for color routing. *Light Sci. Appl.* **2017**, *6*, e17017. [CrossRef] [PubMed]
43. Zhu, L.; Dong, L. Electromagnetically induced transparency metamaterials: Theories, designs and applications. *J. Phys. D Appl. Phys.* **2022**, *55*, 263003. [CrossRef]
44. Zhang, B.; Dong, A.; Wang, J.; Qin, M.; Liu, J.-q.; Huang, W.; Xiao, S.; Li, H. Strong Coupling and Electromagnetically Induced Transparency in Multiple-BIC-Driven Metasurfaces. *Nano Lett.* **2025**, *25*, 4568–4575. [CrossRef]
45. He, F.; Liu, J.; Pan, G.; Shu, F.; Jing, X.; Hong, Z. Analogue of Electromagnetically Induced Transparency in an All-Dielectric Double-Layer Metasurface Based on Bound States in the Continuum. *Nanomaterials* **2021**, *11*, 2343. [CrossRef]
46. Li, J.-S.; Xue, Y.-Y.; Guo, F.-L. Triple frequency bands terahertz metasurface sensor based on EIT and BIC effects. *Opt. Commun.* **2024**, *554*, 130225. [CrossRef]

47. Liu, S.; Xu, Z.; Yin, X.; Zhao, H. Analog of multiple electromagnetically induced transparency using double-layered metasurfaces. *Sci. Rep.* **2020**, *10*, 8469. [CrossRef]
48. Kravets, V.G.; Kabashin, A.V.; Barnes, W.L.; Grigorenko, A.N. Plasmonic Surface Lattice Resonances: A Review of Properties and Applications. *Chem. Rev.* **2018**, *118*, 5912–5951. [CrossRef]
49. Saadatmand, S.B.; Ahmadi, V.; Hamidi, S.M. Quasi-BIC based all-dielectric metasurfaces for ultra-sensitive refractive index and temperature sensing. *Sci. Rep.* **2023**, *13*, 20625. [CrossRef]
50. Xiao, Q.; Fan, L.H.; Ma, Q.; Ning, Y.M.; Gu, Z.; Chen, L.; Li, L.; You, J.W.; Niu, Y.F.; Cui, T.J. Secure wireless communication of brain–computer interface and mind control of smart devices enabled by space-time-coding metasurface. *Nat. Commun.* **2025**, *16*, 7914. [CrossRef] [PubMed]
51. Zhang, W.; Li, J.; Xing, Y.; Nie, X.; Lang, F.; Yang, S.; Hou, X.; Zhao, C. Experimental Study on the Thickness-Dependent Hardness of SiO2 Thin Films Using Nanoindentation. *Coatings* **2021**, *11*, 23. [CrossRef]
52. Wu, H.; Liu, C.; Zhu, Z.; Shao, Y.; Lin, J.; Wen, J.; Wang, H.; Zhang, Y.; Liang, T.; Shao, Y.; et al. Nanoporous Silicon Dioxide Films for Large Area and Low-Cost Fabrication of Ultra-Low Refractive Index Coatings. *ACS Appl. Nano Mater.* **2023**, *6*, 15437–15444. [CrossRef]
53. Fedotova, A.; Younesi, M.; Sautter, J.; Vaskin, A.; Löchner, F.J.F.; Steinert, M.; Geiss, R.; Pertsch, T.; Staude, I.; Setzpfandt, F. Second-Harmonic Generation in Resonant Nonlinear Metasurfaces Based on Lithium Niobate. *Nano Lett.* **2020**, *20*, 8608–8614. [CrossRef] [PubMed]
54. Santiago-Cruz, T.; Fedotova, A.; Sultanov, V.; Weissflog, M.A.; Arslan, D.; Younesi, M.; Pertsch, T.; Staude, I.; Setzpfandt, F.; Chekhova, M. Photon Pairs from Resonant Metasurfaces. *Nano Lett.* **2021**, *21*, 4423–4429. [CrossRef]
55. Fan, Y.; Wang, C.; Tian, H.; Chen, X.; Li, B.Q.; Wang, Z.; Li, X.; Chen, X.; Shao, J. Electric-Field-Driven Generative Nanoimprinting for Tilted Metasurface Nanostructures. *Nano-Micro Lett.* **2025**, *18*, 12. [CrossRef]
56. Tang, Q.; Yao, H.; Xu, B.; Ge, J.; Xu, Y.; Gao, K. Towards high-efficiency Al-BSF c-Si solar cell with both superior omnidirectional and electrical performance by modulating the tilt angle of quasi-periodic inverted pyramid arrays. *Sol. Energy Mater. Sol. Cells* **2022**, *237*, 111576. [CrossRef]
57. Pérez, L.A.; Hu, J.; Mendoza-Carreño, J.; Garriga, M.; Alonso, M.I.; Arteaga, O.; Goñi, A.R.; Mihi, A. Strong Chiro-Optical Activity of Plasmonic Metasurfaces with Inverted Pyramid Arrays. *ACS Appl. Mater. Interfaces* **2025**, *17*, 15824–15835. [CrossRef]
58. Liu, Z.; Xu, Y.; Lin, Y.; Xiang, J.; Feng, T.; Cao, Q.; Li, J.; Lan, S.; Liu, J. High-Q Quasibound States in the Continuum for Nonlinear Metasurfaces. *Phys. Rev. Lett.* **2019**, *123*, 253901. [CrossRef]
59. Gölz, T.; Baù, E.; Aigner, A.; Mancini, A.; Barkey, M.; Keilmann, F.; Maier, S.A.; Tittl, A. Revealing Mode Formation in Quasi-Bound States in the Continuum Metasurfaces via Near-Field Optical Microscopy. *Adv. Mater.* **2024**, *36*, 2405978. [CrossRef]
60. Rosas, S.; Adi, W.; Beisenova, A.; Biswas, S.K.; Kuruoglu, F.; Mei, H.; Kats, M.A.; Czaplewski, D.A.; Kivshar, Y.S.; Yesilkoy, F. Enhanced biochemical sensing with high-Q transmission resonances in free-standing membrane metasurfaces. *Optica* **2025**, *12*, 178–189. [CrossRef] [PubMed]
61. Laskar, A.W.; Adhikary, P.; Singh, N.; Ghosh, S. Coherence as an indicator to discern electromagnetically induced transparency and Autler–Townes splitting. *J. Opt. Soc. Am. B* **2024**, *41*, 29–35. [CrossRef]
62. Fan, S.; Suh, W.; Joannopoulos, J.D. Temporal coupled-mode theory for the Fano resonance in optical resonators. *J. Opt. Soc. Am. A* **2003**, *20*, 569–572. [CrossRef]
63. Haus, H.A.; Huang, W. Coupled-mode theory. *Proc. IEEE* **1991**, *79*, 1505–1518. [CrossRef]
64. Overvig, A.; Mann, S.A.; Alù, A. Spatio-temporal coupled mode theory for nonlocal metasurfaces. *Light Sci. Appl.* **2024**, *13*, 28. [CrossRef]
65. Fan, S.; Joannopoulos, J.D. Analysis of guided resonances in photonic crystal slabs. *Phys. Rev. B* **2002**, *65*, 235112. [CrossRef]
66. Weiss, T.; Muljarov, E.A. How to calculate the pole expansion of the optical scattering matrix from the resonant states. *Phys. Rev. B* **2018**, *98*, 085433. [CrossRef]
67. Peng, B.; Özdemir, Ş.K.; Chen, W.; Nori, F.; Yang, L. What is and what is not electromagnetically induced transparency in whispering-gallery microcavities. *Nat. Commun.* **2014**, *5*, 5082. [CrossRef]
68. Christopoulos, T.; Tsilipakos, O.; Sinatkas, G.; Kriezis, E.E. On the calculation of the quality factor in contemporary photonic resonant structures. *Opt. Express* **2019**, *27*, 14505–14522. [CrossRef]
69. Watanabe, K.; Nagao, T.; Iwanaga, M. Low-Contrast BIC Metasurfaces with Quality Factors Exceeding 100,000. *Nano Lett.* **2025**, *25*, 2777–2784. [CrossRef] [PubMed]
70. Rahimzadegan, A.; Karamanos, T.D.; Alaee, R.; Lamprianidis, A.G.; Beutel, D.; Boyd, R.W.; Rockstuhl, C. A Comprehensive Multipolar Theory for Periodic Metasurfaces. *Adv. Opt. Mater.* **2022**, *10*, 2102059. [CrossRef]
71. Kaelberer, T.; Fedotov, V.A.; Papasimakis, N.; Tsai, D.P.; Zheludev, N.I. Toroidal Dipolar Response in a Metamaterial. *Science* **2010**, *330*, 1510–1512. [CrossRef]
72. Basharin, A.A.; Kafesaki, M.; Economou, E.N.; Soukoulis, C.M.; Fedotov, V.A.; Savinov, V.; Zheludev, N.I. Dielectric Metamaterials with Toroidal Dipolar Response. *Phys. Rev. X* **2015**, *5*, 011036. [CrossRef]

73. Luo, X.-Q.; Zhou, Y.; Liu, Q.; Lu, Z.; Chen, S.; Li, Y.; Liu, W.M. Customizable dual-resonance sensing empowered by coupled quasi-bound states in the continuum. *Opt. Laser Technol.* **2025**, *180*, 111544. [CrossRef]
74. Hu, H.; Lu, W.; Antonov, A.; Berté, R.; Maier, S.A.; Tittl, A. Environmental permittivity-asymmetric BIC metasurfaces with electrical reconfigurability. *Nat. Commun.* **2024**, *15*, 7050. [CrossRef]
75. Jiang, T.; Bhattacharya, A.; Barkey, M.; Aigner, A.; Rohrer, L.; Weber, T.; Wang, J.; Maier, S.A.; Tittl, A. A Comparative Analysis of Plasmonic and Dielectric Metasurface Sensing Platforms Powered by Bound States in the Continuum. *Adv. Funct. Mater.* **2026**, *36*, e16021. [CrossRef]
76. Li, N.; Chen, H.; Zhao, Y.; Wang, Y.; Su, Z.; Liu, Y.; Huang, L. Ultrasensitive metasurface sensor based on quasi-bound states in the continuum. *Nanophotonics* **2025**, *14*, 485–494. [CrossRef]
77. Saadatmand, S.B.; Shokouhi, S.; Ahmadi, V.; Hamidi, S.M. Design and analysis of a flexible Ruddlesden–Popper 2D perovskite metastructure based on symmetry-protected THz-bound states in the continuum. *Sci. Rep.* **2023**, *13*, 22411. [CrossRef]
78. Chen, W.; Li, M.; Zhang, W.; Chen, Y. Dual-resonance sensing for environmental refractive index based on quasi-BIC states in all-dielectric metasurface. *Nanophotonics* **2023**, *12*, 1147–1157. [CrossRef]
79. Chen, C.; Gao, P.; Dai, Y.; Cui, H.; Wang, X.; Huang, T.; Zhu, X.; Liu, H. All-Dielectric Near-Infrared Metasurface with Field Enhancement and High Q-Factor Based on Anapole Precise Manipulation. *Adv. Opt. Mater.* **2025**, *13*, 2403312. [CrossRef]
80. Qiu, S.; Zhang, H.; Shi, Z.; Li, H.; Zhou, Z.-K. Ultrasensitive Refractive Index Sensing Based on Hybrid High-Q Metasurfaces. *J. Phys. Chem. C* **2023**, *127*, 8263–8270. [CrossRef]
81. Sarkar, S.; Zubair, A. Multipolar origin and polarization-controlled high-Q quasi-BIC Fano resonances in dielectric metasurfaces for sensing applications. *Nanoscale Adv.* **2026**, *8*, 1386–1399. [CrossRef] [PubMed]


**Disclaimer/Publisher's Note:** The statements, opinions and data contained in all publications are solely those of the individual author(s) and contributor(s) and not of MDPI and/or the editor(s). MDPI and/or the editor(s) disclaim responsibility for any injury to people or property resulting from any ideas, methods, instructions or products referred to in the content.